




Aerodynamic shape optimization at low Reynolds number using multi-level hierarchical Kriging models

K. Sathyandra Rao^{1,2} · A. N. Abhilasha^{1,3} · Adrija Das^{1,4} · M. Sivapragasam¹ 

Received: 25 March 2024 / Accepted: 12 August 2024

© The Author(s), under exclusive licence to Springer Science+Business Media, LLC, part of Springer Nature 2024

Abstract

The aerodynamic performance characteristics of an unmanned aerial vehicle airfoil and wing are optimized in the low Reynolds number regime using a variable-fidelity Multi-Level Hierarchical Kriging (MHK) surrogate modeling framework. This methodology employs aerodynamic data obtained from computational grids of varying grid resolution. This approach results in an efficient framework for optimizing expensive aerodynamic functions with the aid of lower fidelity data. The MHK-based optimization framework is first applied to enhance the aerodynamic properties of an Eppler E214 airfoil. The endurance factor of the airfoil is improved by 28%. Next, the aerodynamic characteristics of a small unmanned aerial vehicle wing is optimized. The endurance factor of the optimal wing is improved by 12.5%, with a substantial 45 drag count reduction. The optimal wing is of a swept wing design with a leading edge sweep of 13.6°. The evolution of a swept wing as the optimal wing design is an interesting outcome of the present study. Though the effect of wing sweep is well studied in high-subsonic and supersonic flows, its effect in the incompressible low Reynolds number regime is quantified in the present study. The wing sweep increases the suction on the outboard portion of the wing leading to a higher lift coefficient of the optimal wing. Further, the drag coefficient of the optimal wing is also reduced compared to the baseline wing. Much of this drag reduction comes from the reduction in the pressure drag component. Thus the wing sweep not only increases the lift coefficient, but also decreases the drag coefficient. This leads to a significant increase in the lift-to-drag

✉ M. Sivapragasam
sivapragasam.aae.et@msruas.ac.in

¹ Department of Aerospace and Automotive Engineering, Faculty of Engineering and Technology, M S Ramaiah University of Applied Sciences, Bangalore 560 058, India

² Present Address: Avionics Software and Systems Testing, Airbus Group India Private Limited, Bangalore 560 048, India

³ Present Address: Aerodynamics and Performance Department, Aeronautical Development Agency, Bangalore 560 017, India

⁴ Present Address: Defence Department, Kalyani Strategic Systems Limited, Pune 411036, India

ratio and the endurance factor of the optimal wing design. The present results demonstrate the optimization efficiency of the MHK modeling approach in the sensitive low Reynolds number regime.

Keywords Low Reynolds number flow · Laminar-turbulent transition · Aerodynamic shape optimization · Surrogate modeling · Hierarchical Kriging

1 Introduction

Unmanned Aerial Vehicles (UAV) are employed for a variety of civilian and military applications. Austin (2010), Gundlach (2012), Jayaraman (2014) and Marshall et al. (2016) are excellent compendiums on unmanned aircraft design and technologies. Small/mini UAVs are gaining much importance recently since they are portable and can be easily deployed by hand launch. The small Unmanned Aircraft Systems or sUAS, as classified by the US Department of Defense as Group 1 and Group 2, are categorized with maximum gross take-off weight under 55 lbs (25 kg), normal operating altitude less than 3500 ft (1066.8 m) above ground level and air speed less than 250 knots (128.6 m/s).

The small unmanned air vehicles and micro air vehicles operate in the low Reynolds number regime, $O(10^5)$. The Reynolds number $Re \equiv Uc/\nu$, is based on the flight velocity U and wing chord length c , and ν is the fluid kinematic viscosity. In this Reynolds number regime, the maximum achievable lift coefficients are lower, and the drag coefficient values are higher than high Reynolds number vehicles. Consequently, the maximum lift-to-drag ratio values are lower by more than an order of magnitude. Low Reynolds number operation is also of interest for small-scale wind turbines, low-pressure turbines of gas turbine engines, and more recently, powered flight in the Martian atmosphere. These engineering applications necessitate an enhanced understanding of low Reynolds number flows for improving their aerodynamic efficiency.

At low Reynolds numbers, the laminar boundary layer on the airfoil upper surface separates due to an adverse pressure gradient. The separated shear layer is unstable to small disturbances and transitions to turbulence via the Kelvin–Helmholtz instability mechanism. The transitioned shear layer could reattach on the airfoil surface well ahead of the airfoil trailing edge and a turbulent boundary layer subsequently develops on the airfoil surface. This flow system of laminar separation, transition to turbulence, and turbulent reattachment is referred to as a Laminar Separation Bubble (LSB) (Tani 1964; Gaster 1967; Horton 1968; Carmichael 1981; Lissaman 1983). The LSB occupies a substantial proportion of the airfoil chord length and alters the aerodynamic characteristics of the airfoil compared to inviscid flow (Mueller et al. 2003). Further, the LSB is extremely sensitive to changes in airfoil geometry and changes in Reynolds number or freestream turbulence intensity (Shyy et al. 2008). The designers of UAVs and MAVs, therefore, have a challenging task of designing aerodynamically efficient lifting surfaces for enhanced flight performance.

Optimization methods are employed to improve the aerodynamic characteristics of airfoils and wings. Some of the early work in aerodynamic optimization employed gradient-based methods (Hicks and Henne 1978; Jameson 1988). It is well-known

that these methods often get trapped into a local optima and also the optimal solutions depend on the initial design. Attempts to alleviate these drawbacks led to the development of evolutionary optimization algorithms that can obtain global optimum. However, directly coupling such optimization algorithms with high-fidelity computational codes is computationally prohibitive since a very large number of function evaluations are required to achieve the global optimum. Surrogate-based optimization methods are useful in such contexts. In these methods a select number of high-fidelity computations are performed and a surrogate model is constructed using this dataset; then the surrogate model is subjected to the optimizer in lieu of direct high-fidelity evaluations, thereby reducing the computational cost of the optimization process (Jones et al. 1988; He et al. 2020; Qui et al. 2022). Due to a large number of design variables involved in engineering optimization problems and also due to the fact that high-fidelity computations are required to evaluate the function response, the construction of a surrogate model itself is computationally demanding. Therefore, there is a need to reduce the computational cost of the optimization process but still retain high-fidelity information in the surrogate models. Multiple-fidelity modeling can be employed to overcome these challenges. Kriging models are very popular in the engineering optimization community for surrogate modeling (Krige 1951; Sacks et al. 1989; Queipo et al. 2005; Jones 2001; Forrester et al. 2008; Forrester et al. 2009). These models generally employ a single-level of fidelity. Co-Kriging models proposed by Kennedy and O'Hagan (2000), Forrester et al. (2007) and Zadeh et al. (2016) employ two-levels of fidelity. Han and Goertz (2012) and Han et al. (2020) proposed a Multi-Level Hierarchical Kriging (MHK) modeling approach that employs arbitrary levels of fidelity data. This procedure was found to be computationally efficient in aerodynamic shape optimization.

Several optimization techniques have been applied for aerodynamic optimization in the past. However, aerodynamic shape optimization in the low Reynolds number regime involving laminar-turbulent flow transition have been limited. Amoignon et al. (2006) solved the parabolized stability equations to predict the transition location, and used the adjoint method to optimize the aerodynamic coefficients of RAE 2822 airfoil. Driver and Zingg (2007) used the e^N method for transition prediction, and the discrete-adjoint algorithm for optimization. Lee and Jameson (2009) applied the e^N method for transition prediction, and employed the gradient-based continuous adjoint method for optimizing natural-laminar-flow airfoil and wing. Cameron et al. (2011) performed a global optimization of natural-laminar-flow airfoil using e^N method and linear stability theory for transition prediction. Khayat-zadeh and Nadarajah (2012) used the $\gamma-Re_\theta$ transition model and an adjoint-based shape optimization procedure for optimizing natural-laminar-flow airfoil. Rashad and Zingg (2016) also used the e^N method for transition prediction, and sequential quadratic programming for optimization. Han et al. (2012) performed design optimization of laminar supercritical airfoils using a surrogate-based approach; e^N transition method was employed by them. Zhang et al. (2015) performed aerodynamic optimization of supercritical natural-laminar-flow airfoil using the $\gamma-Re_\theta$ transition model. Han et al. (2018) employed the full e^N method that accounts both Tollmien-Schlichting and crossflow instabilities for transition prediction; their optimizer was a Kriging surrogate model. Chi et al. (2019)

performed inverse design and direct optimization of transonic natural laminar flow airfoils using surrogate-based optimization. Halila et al. (2020) performed aerodynamic shape optimization by an adjoint-based method; their flow solver is RANS coupled with amplification factor transport model for transition prediction. Shi et al. (2020, 2021) employed a discrete adjoint methodology to optimize natural laminar flow airfoil and wing. Wauters and Degroote (2021) used the $\gamma-Re_\theta$ transition model and regressive co-Kriging surrogate model to optimize the wing fence of an UAV. Arshad et al. (2021) used modeFRONTIER optimization package and XFOIL aerodynamics solver to optimize the SG6043 airfoil. Wang and Guo (2022) optimized natural laminar flow airfoil for surface contamination conditions using non-dominated sorting genetic algorithm—II and Monte Carlo simulation with XFOIL as the aerodynamics solver. Sabater et al. (2022) performed a robust design optimization of transonic natural laminar flow wing using a surrogate based optimization strategy. Piotrowski and Zingg (2022) used a local correlation-based transition model in conjunction with RANS-based Newton–Krylov flow solver and discrete-adjoint gradient-based optimization algorithm to minimize the drag of airfoils. Nie et al. (2022) presented a surrogate-based e^N method for compressible boundary layers to be used in lieu of linear stability analysis. The results were demonstrated on NLF-0416 and NPU-LSC-72613 airfoils. Chen et al. (2023) performed robust optimization using adjoint-based method to design laminar flow airfoils under uncertainties due to flight conditions. Yan et al. (2023) optimized a natural laminar flow nacelle in transonic flow using a differential evolution algorithm combined with a radial basis function; transition was modeled using the $\gamma-Re_\theta$ transition. Sudhi et al. (2023) used multi-objective genetic algorithm to optimize natural laminar flow and hybrid laminar flow airfoils. The Euler flow solver integrated with boundary-layer coupling was used for flowfield and linear stability analysis was used for transition prediction. Li et al. (2022) used the three-equation transition model and optimized the performance of S809 and NLF0416 airfoils. Yu et al. (2023) optimized the aerodynamic performance of FX63-137 airfoil for solar powered unmanned aerial vehicle application using the $k-k_L-\omega$ and $\gamma-Re_\theta$ transition models.

It is seen that most of the existing work have focussed on design optimization of two-dimensional airfoils. Only a few studies have dealt with three-dimensional wing optimization. Further, these studies have considered flows at high Reynolds numbers, and high transonic Mach numbers relevant to commercial transport aircraft. Aerodynamic shape optimization at low Reynolds numbers of design relevance to UAVs and MAVs have not been considered in the past and is the focus of the present study.

The present work is further motivated by the need for an efficient aerodynamic shape optimization methodology in the sensitive low Reynolds number regime. Our previous work in the low Reynolds number domain employed co-Kriging surrogate models for optimization (Pranesh et al. 2018; Priyanka and Sivapragasam 2021; Das and Sivapragasam 2024). We had obtained significant improvements in the aerodynamic performance using this modeling approach. The Multi-Level Hierarchical Kriging (MHK) modeling approach of Han et al. (2020) forms the basis of the present work. Recently, Zhang et al. (2024) proposed a multi-fidelity expected improvement criterion based on the multi-level hierarchical kriging model approach to select new samples

of arbitrary fidelity levels and update the MHK models. Another interesting application of hierarchical Kriging was recently proposed by Xu et al. (2024). The expert’s experience-informed hierarchical kriging (EEI-HK) model is built in a sequential manner and was found to improve the prediction accuracy of the aerodynamics model. In the present study, we implement the MHK modeling methodology and demonstrate its effectiveness using an analytical test function. Then, this methodology is applied to aerodynamic shape optimization of an Eppler E214 airfoil, and an UAV wing at a low Reynolds number involving laminar to turbulent flow transition.

2 Multi-level hierarchical Kriging modeling

In this section, the mathematical modeling of Multi-Level Hierarchical Kriging (MHK) is presented briefly. Suppose that for a chosen m -dimensional problem, with \mathbf{x} as the vector of design variables, the prediction of an expensive high-fidelity function

$$y_1 = f_1(\mathbf{x}) \tag{1}$$

where $y_1: \mathbb{R}^m \rightarrow \mathbb{R}$, is to be accomplished with the aid of inexpensive lower-fidelity functions

$$y_k = f_k(\mathbf{x}), \quad k = 2, 3, \dots, L \tag{2}$$

where $y_k: \mathbb{R}^m \rightarrow \mathbb{R}$. k denotes the k^{th} level of fidelity, with $k = 1$ being the highest level fidelity, and $k = L$ the lowest level fidelity. The high-fidelity function is sampled at $\mathbf{S}_1 = [\mathbf{x}_1^{(1)}, \mathbf{x}_1^{(2)}, \dots, \mathbf{x}_1^{(n_1)}]^T \in \mathbb{R}^{n_1 \times m}$ with the corresponding responses being $\mathbf{y}_1 = [y_1^{(1)}, y_1^{(2)}, \dots, y_1^{(n_1)}]^T \in \mathbb{R}^{n_1}$. Similarly, the lower fidelity functions are sampled at $\mathbf{S}_k = [\mathbf{x}_k^{(1)}, \mathbf{x}_k^{(2)}, \dots, \mathbf{x}_k^{(n_k)}]^T \in \mathbb{R}^{n_k \times m}$, and their responses being $\mathbf{y}_{S,k} = [y_k^{(1)}, y_k^{(2)}, \dots, y_k^{(n_k)}]^T \in \mathbb{R}^{n_k}$. In order to limit the number of high-fidelity evaluations, $n_1 \ll n_2 \ll \dots \ll n_L$. We now have the high-fidelity $(\mathbf{S}_1, \mathbf{y}_1)$, and lower-fidelity $(\mathbf{S}_k, \mathbf{y}_{S,k})$ datasets in the vector space. Then, the task at hand is to develop an approximation model using these datasets to quickly predict the high-fidelity response at any untried location $\mathbf{x} \in \mathbb{R}^m$.

The multi-level hierarchical Kriging model is formulated as

$$Y_k(\mathbf{x}) = \begin{cases} \beta_k + Z_k(\mathbf{x}) & k = L \text{ for the lowest level fidelity} \\ \beta_k \hat{y}_{k+1}(\mathbf{x}) + Z_k(\mathbf{x}) & k = L - 1, L - 2, \dots, N \end{cases} \tag{3}$$

It may be noted that with $k = L$, i.e., the lowest level fidelity, the above expression is a pure Kriging model. However, for higher levels of fidelity, $L-1, L-2, \dots, N$, the Kriging models are constructed in a recursive manner using a lower-fidelity Kriging model $\hat{y}_{k+1}(\mathbf{x})$ scaled by an unknown constant β_k that serves as a model trend. $Z_k(\mathbf{x})$ is a Gaussian random process representing the k^{th} level fidelity. The predictor for the k^{th} level of fidelity is

$$\hat{y}_k(\mathbf{x}) = \beta_k \hat{y}_{k+1}(\mathbf{x}) + \mathbf{r}_k^T(\mathbf{x}) \mathbf{R}_k^{-1} (y_{S,k} - \beta_k \mathbf{F}_k) \tag{4}$$

In Eq. (4), the spatial correlation function \mathbf{R}_k , the correlation vector representing the correlation between the untried point and the observed points \mathbf{r}_k , and the regression matrix of the Kriging predictor \mathbf{F}_k are defined as follows:

$$\mathbf{R}_k := \left(R\left(\theta_k, \mathbf{x}_k^{(i)}, \mathbf{x}_k^{(j)}\right) \right)_{i,j} \in \mathbb{R}^{n_k \times n_k} \quad (5)$$

$$\mathbf{r}_k := \left(R\left(\theta_k, \mathbf{x}_k^{(i)}, \mathbf{x}\right) \right)_i \in \mathbb{R}^{n_k} \quad (6)$$

$$\mathbf{F}_k = \begin{cases} [1, 1, \dots, 1]^T \in \mathbb{R}^{n_k} & k = L, \text{ the lowest level fidelity} \\ \left[\hat{y}_{k+1}\left(\mathbf{x}_k^{(1)}\right), \hat{y}_{k+1}\left(\mathbf{x}_k^{(2)}\right), \dots, \hat{y}_{k+1}\left(\mathbf{x}_k^{(n_k)}\right) \right]^T \in \mathbb{R}^{n_k} & \text{otherwise} \end{cases} \quad (7)$$

In Eqs. (5–7), θ_k are the hyperparameter vectors for spatial correlation functions. In the present study, the hyperparameters of each of the Kriging models are determined by maximizing the concentrated log-likelihood function (Toal et al. 2008). The scaling factor β_k representing the degree of correlation between two models of adjacent levels of fidelity is evaluated as

$$\beta_k = \left(\mathbf{F}_k^T \mathbf{R}_k^{-1} \mathbf{F}_k \right)^{-1} \mathbf{F}_k^T \mathbf{R}_k^{-1} \mathbf{y}_{S,k}. \quad (8)$$

Finally, the predictor of the MHK model is

$$\hat{y}_1(\mathbf{x}) = \prod_{k=1}^L \beta_k + \sum_{k=1}^L \left[\prod_{i=1}^{k-1} \beta_i \mathbf{K}_k(\mathbf{x}) \right] + \mathbf{K}_1(\mathbf{x}) \quad (9)$$

where the first term on the right-hand side represents the global trend of the MHK model, and the second term represents the trend of the low-fidelity data. $\mathbf{K}_k(\mathbf{x})$ is defined as

$$\mathbf{K}_k(\mathbf{x}) = \mathbf{r}_k^T(\mathbf{x}) \mathbf{R}_k^{-1} (\mathbf{y}_{S,k} - \beta_k \mathbf{F}_k). \quad (10)$$

The procedure for constructing a MHK is as follows. First, a Kriging model of the lowest fidelity Y_L is built using the dataset $(\mathbf{S}_L, \mathbf{y}_{S,L})$. Then, using Y_L as a model trend, a Kriging model of the next higher level fidelity Y_{L-1} is built using the dataset $(\mathbf{S}_{L-1}, \mathbf{y}_{S,L-1})$. In a similar manner, the Kriging models of higher level fidelities $Y_{L-2}, Y_{L-1}, \dots, Y_2$ are built using the datasets $(\mathbf{S}_{L-2}, \mathbf{y}_{S,L-2}), (\mathbf{S}_{L-3}, \mathbf{y}_{S,L-3}), \dots, (\mathbf{S}_2, \mathbf{y}_2)$, respectively. Finally, the Kriging model of the highest fidelity Y_1 is built using the dataset $(\mathbf{S}_1, \mathbf{y}_1)$.

3 Optimization methodology using MHK models

3.1 MHK optimization methodology

A general constrained high-fidelity optimization problem with the aid of lower-level fidelity analyses can be formulated as follows:

$$\begin{aligned}
 & \min y_1(\mathbf{x}) \\
 & \text{s. t. } g_{1,i}(\mathbf{x}) \leq 0, \quad i = 1, 2, \dots, N_c \\
 & \text{using } y_k(\mathbf{x}) \text{ and } g_{k,i}(\mathbf{x}), \quad k = 2, 3, \dots, L \\
 & \mathbf{x}_l \leq \mathbf{x} \leq \mathbf{x}_u
 \end{aligned} \tag{11}$$

where $y_1(\mathbf{x})$ and $g_{1,i}(\mathbf{x})$ are the high-fidelity objective and constraint functions, respectively; $y_k(\mathbf{x})$ and $g_{k,i}(\mathbf{x})$ are the lower-fidelity objective and constraint functions, respectively. There are a total of L levels of fidelity, and N_c number of constraint functions. \mathbf{x}_l and \mathbf{x}_u are the lower and upper bounds, respectively, of the design variables \mathbf{x} .

The MHK-based optimization methodology is listed in the following steps:

- (1) Design space sampling: A suitable Design of Experiments (DoE) method is employed to sample the L levels of fidelity. A very large number of low-fidelity samples are selected with decreasing number of samples chosen with increasing level of fidelity.
- (2) High- and lower-fidelity function evaluations: For the chosen samples, the function responses are evaluated using the appropriate high- and lower-fidelity numerical simulations.
- (3) MHK model building: A Kriging model of the lowest fidelity is first built, followed by successive builds of Kriging models each one using the model trend of the previous lower level fidelity till the Kriging model of the highest fidelity is built.
- (4) Infill sampling: A suitable infill sampling technique is employed to select the new samples for the high-fidelity Kriging model.
- (5) Model update: High-fidelity function evaluation is done at the new sample and the MHK models are updated.
- (6) Termination: Steps (2–5) are repeated until a termination condition is satisfied.

This process is illustrated by means of a flowchart in Fig. 1.

3.2 Demonstration of the MHK optimization methodology

The Branin function is chosen as the test case to demonstrate the effectiveness of the optimization methodology discussed in the previous section. In particular, we choose the forms of the Branin function and the lower fidelity functions used in Perdikaris

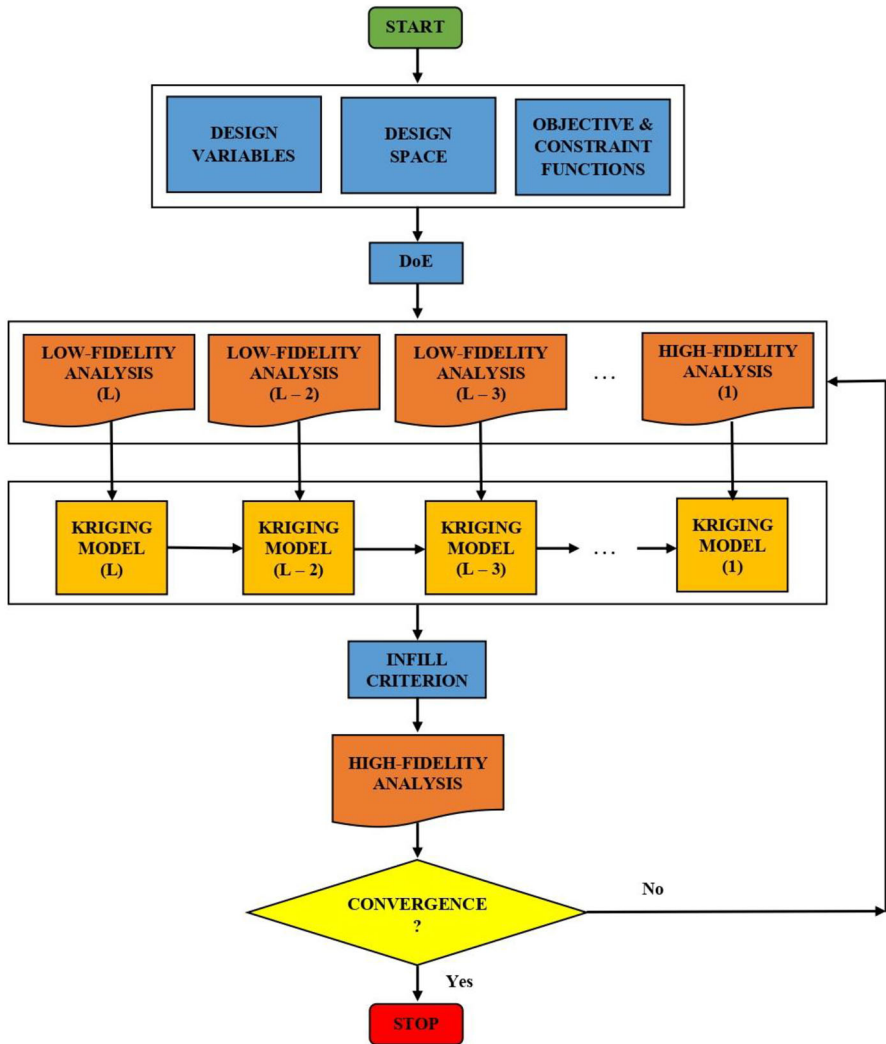


Fig. 1 Flowchart of MHK-based optimization process (adapted from Han et al. 2020)

et al. (2017). The mathematical formulation of the minimization of the Branin function is

$$\begin{aligned} \min y_1 &\equiv f(\mathbf{x}) \\ &= \left(\frac{-1.275x_1^2}{\pi^2} + \frac{5x_1}{\pi} + x_2 - 6 \right)^2 + \left(10 - \frac{5}{4\pi} \right) \cos x_1 + 10 \end{aligned}$$

$$\text{using } y_2 = 10\sqrt{y_1(x-2)} + 2(x_1 - 0.5) - 3(3x_2 - 1) - 1$$

$$y_3 = y_2 [1.2(x + 2)] - 3x_2 + 1$$

$$x_1 \in [-5, 10], x_2 \in [0, 15] \tag{12}$$

Here, y_1 is the high-fidelity function whose optimum is to be obtained with the aid of a medium- fidelity function y_2 , and a low-fidelity function y_3 . The global minimum of the high-fidelity Branin function y_1 is $f(\mathbf{x}^*) = 0.397887$, at $\mathbf{x}^* = (-\pi, 12.275), (\pi, 2.275)$ and $(9.42478, 2.475)$ (Surjanovic and Bingham 2013). The medium- (y_2) and low-fidelity (y_3) functions are obtained by shifting the phase and amplitude, and also by non-uniformly scaling the high-fidelity Branin function. The surface plots of these functions are plotted in Fig. 2. The Pearson’s correlation coefficient values between the high-to-medium, high-to-low and medium-to-low fidelity models are $-0.511, 0.485,$ and $-0.901,$ respectively, using 40 randomly sampled points in x . There is a complex nonlinear spatial cross-correlation between the three functions (Perdikaris et al. 2017), thus making the optimization problem in Eq. (12) a good test case to illustrate the efficiency of the MHK-based optimization methodology.

To assess the performance of the MHK-based optimization, the results of pure Kriging of the high-fidelity function, two-level hierarchical Kriging of the high- and medium-fidelity functions, and finally multi-level hierarchical Kriging of the high-, medium- and low-fidelity functions are compared. The space-filling Latin Hypercube Sampling (LHS) technique of Morris and Mitchell (1995) is used to select the number of samples for low-fidelity (80 samples), medium-fidelity (40 samples) and high-fidelity (10 samples). The function values are evaluated for these many samples using their respective functions and the Kriging models are constructed. The models are

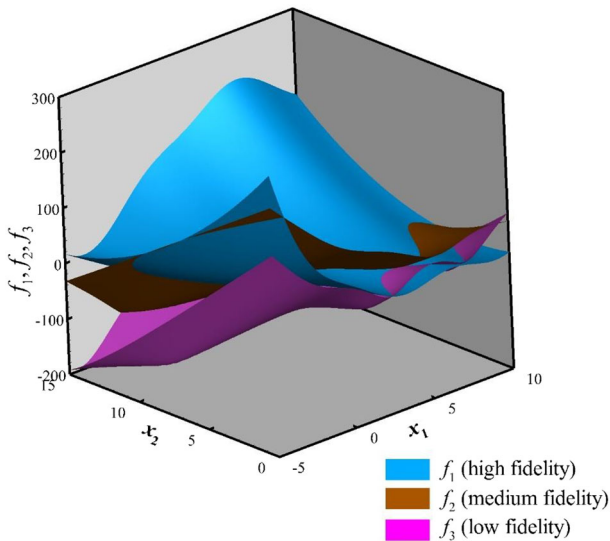


Fig. 2 Contours of high-, medium- and low-fidelity response surfaces the Branin function

subjected to the genetic algorithm optimizer and the optimum obtained. The infill sample points are chosen by maximizing the expected improvement (EI) function (Jones et al. 1998), and the Kriging models are updated using high-fidelity infills. The best-so-far convergence history of the three optimization procedures are plotted in Fig. 3. It is seen that compared to the pure Kriging or the two-level hierarchical Kriging models, the three-level MHK model leads to faster convergence and also with lesser number of high-fidelity function evaluations. Further, the three-level MHK results in better convergence with the relative error defined as $|\hat{f}(\mathbf{x}^*) - f(\mathbf{x}^*)|/f(\mathbf{x}^*)$, dropping below 10^{-8} , better than the other two models; here $f(\mathbf{x}^*)$ is the global optimum and $\hat{f}(\mathbf{x}^*)$ is the predicted optimum. The results are summarized in Table 1. It is clear that the usage of a three-level MHK model in the optimization process is advantageous

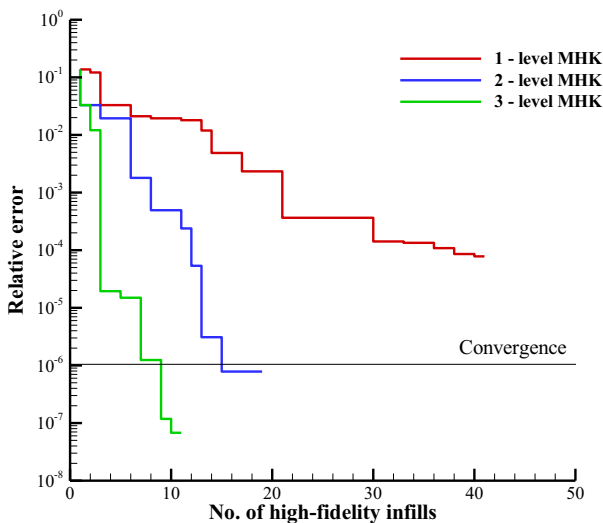


Fig. 3 Comparison of convergence of the three MHK models

Table 1 Summary of optimization of Branin function

Optimization method	Number of initial samples			Number of high-fidelity infills	Optimum	Relative error
	y_1	y_2	y_3			
Pure Kriging	10			41	0.397915966	7.28×10^{-5}
Two-level hierarchical Kriging	10	40		19	0.397887312	7.83×10^{-7}
Three-level hierarchical Kriging	10	40	80	11	0.397887027	6.78×10^{-8}

compared to the pure Kriging or the two-level hierarchical Kriging models. Finally, we mention that in the analytical test case chosen here and also in the aerodynamic shape optimization problems in Sect. 4, we have employed three levels of fidelity since it was deemed sufficient in Han et al. (2020). However, the MHK modeling approach can readily be extended to arbitrary levels of fidelity, if such datasets are available.

4 Aerodynamic shape optimization at low Reynolds number

The efficacy of the MHK model-based optimization approach was established in Sect. 3.2. We now apply this methodology for aerodynamic shape optimization at a low Reynolds number involving laminar to turbulent boundary layer transition. These problems pertain to maximizing the endurance factor of an airfoil, and then the wing of a small UAV. The endurance factor is chosen as the objective function here since it is one of the key design drivers for small UAV class of vehicles (Austin 2010).

4.1 Maximization of endurance factor of Eppler E214 airfoil

The first problem is the maximization of the endurance factor of an Eppler E214 airfoil at a Reynolds number, based on the airfoil chord length and cruise velocity, $Re = 2.8 \times 10^5$, and at a freestream turbulence intensity of $Tu = 0.1\%$. The angle of attack is set to $\alpha = 2.5^\circ$. The E214 airfoil is a popular choice for small remotely piloted and autonomous air vehicles. It is designed with a laminar separation ramp leading to mild pressure recovery on the aft of the upper surface (Selig et al. 1989). This airfoil has a maximum thickness of 11.10% at 32.14% chord location, and a maximum camber of 4.03% at 53.16% chord location. The relatively large amount of aft camber is an interesting geometric feature of this airfoil.

The aerodynamic optimization problem is posed as

$$\begin{aligned} & \max \left(\frac{C_l^{3/2}}{C_d} \right) \\ & \text{s. t. } \begin{cases} C_l \geq C_l^* \\ t_{\max} \geq t_{\max}^* \end{cases} \end{aligned} \quad (13)$$

We are to maximize the endurance factor, $C_l^{3/2}/C_d$, of the airfoil subject to two inequality constraints. The first inequality constraint is that the C_l of the optimal airfoil must be greater than or equal to the C_l of the baseline airfoil, C_l^* . We have chosen $C_l^* = 0.75$. The second constraint is that the maximum thickness-to-chord ratio t_{\max} must be greater than or equal to that of the baseline airfoil, $t_{\max}^* = 0.111$. The constraints are handled by penalizing the objective function. It must be mentioned that though the geometric constraints are simpler to handle, the aerodynamic constraints are not. The penalty function approach offers a simple and an efficient way to handle aerodynamic constraints (Leifsson and Koziel 2015), and has been used in the present study.

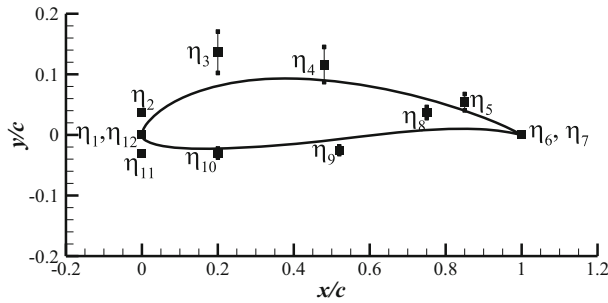


Fig. 4 Bezier representation of Eppler E214 airfoil with control points and their bounds

The E214 airfoil is parameterized using Bezier curves (Samareh 2001). Six control points each are used to represent the upper and lower surfaces of the airfoil separately. The control points η_1 , η_6 , η_7 and η_{12} are fixed to maintain $x/c = 1$. The control points η_2 and η_{11} are fixed to maintain the airfoil leading edge curvature. This leaves six control points (η_3 , η_4 , η_5 , η_8 , η_9 and η_{10}) as design variables for optimization which vary along the y -axis and constitute the vector of design variables. These six control points are allowed to vary by $0.025c$ on either side of the baseline y -coordinate value. This defines the design space for optimization. The control points and their bounds are shown in Fig. 4.

The incompressible Reynolds-averaged Navier–Stokes (RANS) equations

$$\frac{\partial}{\partial x_i} (\rho u_i) = 0 \quad (14)$$

$$\frac{\partial}{\partial x_j} (\rho u_i u_j) = -\frac{\partial p}{\partial x_i} + \frac{\partial}{\partial x_j} \left[\mu \left(\frac{\partial u_i}{\partial x_j} + \frac{\partial u_j}{\partial x_i} - \frac{2}{3} \delta_{ij} \frac{\partial u_l}{\partial x_l} \right) \right] + \frac{\partial}{\partial x_j} (-\rho \overline{u_i' u_j'}) \quad (15)$$

are solved using the CFD code Fluent which employs a finite-volume-based method to obtain the numerical solution. In eqs. (14) and (15), u_i and u_i' are the mean and fluctuating velocity components, respectively, p is the pressure, and ρ and μ are the fluid density and fluid viscosity, respectively, both assumed constant. In Eq. (15), $(-\rho \overline{u_i' u_j'})$ are the Reynolds stresses and are modeled using the Menter shear-stress transport k - ω model (1994). Here k is the turbulence kinetic energy, and ω is the specific dissipation rate of k . The Langtry-Menter γ - $Re_{\theta t}$ transition model (2009) is used for transition prediction. This model uses two transport equations, one for intermittency γ , and another for transition momentum thickness Reynolds number $Re_{\theta t}$.

The computational domain extends $10c$ from the leading edge of the airfoil and $20c$ in the downstream direction as shown in Fig. 5. A structured curvilinear body-fitted grid of the C–H type topology is generated around the airfoil. A large number of grid points are kept close to the airfoil surface to resolve the steep velocity gradients in the boundary layer. It is also ensured that the near wall y^+ is less than 1 for all the

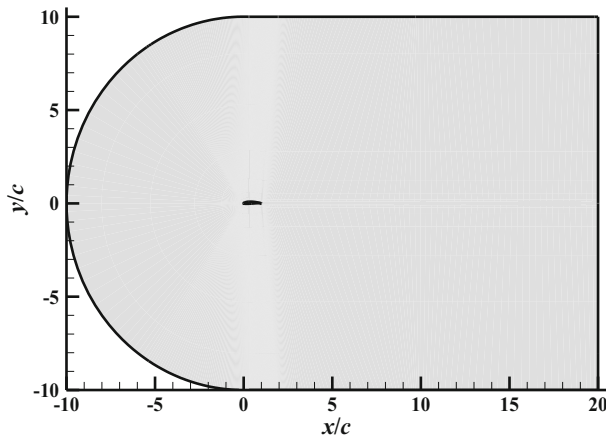


Fig. 5 Computational domain for airfoil computations

simulations. The grid is progressively coarsened away from the airfoil to maintain an acceptable total number of grid points for the computations.

The velocity inlet boundary condition is specified at the inlet of the computational domain. The freestream turbulence intensity is also specified at the inlet. The pressure-outlet boundary condition is specified at the outlet of the computational domain. The no-slip boundary condition is applied on the airfoil surface. The convective terms in the momentum equations are discretized by a second-order accurate upwind scheme, and the viscous terms by a second-order accurate central difference scheme. The pressure values at the cell faces are interpolated using a second-order accurate central differencing scheme. The turbulence and transition model equations are discretized using second-order upwind schemes. The gradients used to discretize the convection and diffusion terms are evaluated by the least-squares cell-based method. The momentum and pressure-based continuity equations are solved in a coupled manner resulting in excellent solution convergence. The numerical calculations are performed in double-precision arithmetic.

The high- and low-fidelity computational analyses are carried out by solving the Reynolds-averaged Navier–Stokes equations along with the SST $k-\omega$ turbulence model and the $\gamma-Re_{\theta t}$ transition model on computational grids of varying grid resolution. Three levels of fidelity are considered in the present optimization. The high-, medium- and low-fidelity grids are determined by performing a careful grid independence study. The high-fidelity grid has 916 grid points around the airfoil surface and 301 in the normal direction; the medium- and low-fidelity grids have 640×206 , and 456×144 grids, respectively. A close-up view of the grid surrounding the airfoil for the three grids is shown in Fig. 6. The $C_l^{3/2}/C_d$ values obtained using the three grids and the computational time required for solution convergence for each of the grids are tabulated in Table 2. The present computational results are validated by comparing with the experimental results of Selig et al. (1989) as shown in Fig. 7. The flow conditions corresponding to the experimental set up are applied for the computations;

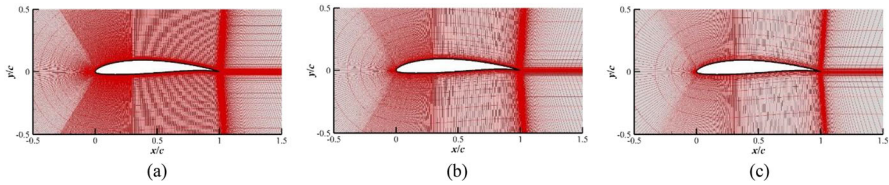


Fig. 6 Computational grids for airfoil; **a** high-, **b** medium-, and **c** low-fidelity grid

Table 2 Summary of airfoil grid independence study; $Re = 2.0 \times 10^5$, $Tu = 0.188\%$, $\alpha = 4^\circ$

Grid	No. of cells	C_l	C_d	$C_l^{3/2}/C_d$	Time (mins)
L1 (high-fidelity grid)	916×301	0.9108	0.01549	56.11	420
L2 (medium-fidelity grid)	640×206	0.9186	0.01472	59.79	300
L3 (low-fidelity grid)	456×144	0.9198	0.01451	60.80	180

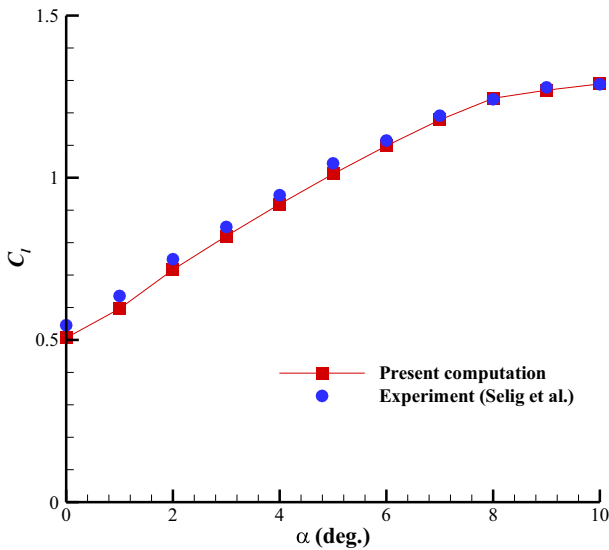


Fig. 7 Comparison of present computational results with experimental data for E214 airfoil

$Re = 2.0 \times 10^5$ and $Tu = 0.188\%$. An excellent agreement is obtained validating the computational procedure.

The LHS technique is used to sample the three fidelity levels. We choose 120 samples for the low-fidelity, 30 samples for the medium-fidelity, and 6 samples for the high-fidelity computations. It must be noted that the number of high-fidelity samples is substantially lower than the medium- and low-fidelity samples. It is indeed the purpose of the MHK to limit the number of high-fidelity evaluations as low as possible.

Surrogate models are built for the endurance factor ($C_l^{3/2}/C_d$) as discussed in Sect. 2. The Pearson’s correlation coefficient values between high-to-medium, high-to-low, and medium-to-low fidelity models are 0.187, 0.647, and 0.229, respectively. There is a positive correlation between the endurance factor values obtained from the different fidelity aerodynamic computations. The GA is employed as the optimization engine. The Expected-Improvement (EI)-based infilling strategy is employed in the current optimization study. The sample point in the design space where an infill must be made is obtained by maximizing the EI function using GA. A high-fidelity computation is performed for every infill sample given by EI. The data is appended to the high-fidelity dataset and the MHK model is built iteratively until the optimal shape is obtained by maximizing the objective function.

The baseline and optimal airfoil geometries are plotted in Fig. 8. The thickness constraint is satisfied in the present optimization procedure. The maximum camber of the optimal airfoil has increased from 4.03% of the baseline to 5.83% for the optimal airfoil. The aerodynamic characteristics of the airfoils are tabulated in Table 3.

The endurance factor of the optimal airfoil has improved by 28% compared to the baseline airfoil. This improvement is due to the increase in the C_l of the optimal airfoil. The C_l of the optimal airfoil has increased by 25.3 lift counts (1 lift count = $10^2 C_l$). The increase in the maximum camber of the optimal airfoil and the delay in flow separation have contributed to this improvement. There is an increase in C_d of the optimal airfoil by 23.3 drag counts (1 drag count = $10^4 C_d$). The increase in C_d is due to the maximum thickness of the optimal airfoil being slightly thicker (11.26%) than the baseline airfoil (11.1%). Another interesting observation is the delay in flow separation of the optimal airfoil. The boundary layer separates at $x_s/c = 0.511$ for the optimal airfoil as compared to $x_s/c = 0.483$ for the baseline airfoil. The flow transition

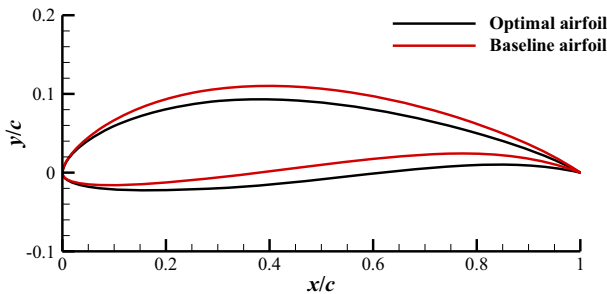


Fig. 8 Comparison of baseline and optimal airfoils

Table 3 Aerodynamic characteristics of baseline and optimal airfoils

Airfoil	C_l	C_d	$C_l^{3/2}/C_d$	x_s/c	x_t/c	x_r/c	l_B
Baseline	0.7500	0.01117	58.15	0.485	0.727	0.744	0.259
Optimal	1.0027	0.01350	74.36	0.511	0.725	0.750	0.239

x_l/c and reattachment x_r/c occur at nearly the same locations for both the airfoils. The net result is a reduction in the length of the LSB l_B for the optimal profile.

The contours of pressure coefficient C_p superimposed over streamlines are plotted in Fig. 9. The laminar separation bubble on the upper surface of the airfoils is shown in the inset in these frames. The C_p distribution over the optimal and baseline airfoils are plotted in Fig. 10. The suction pressure on the upper surface of the optimal airfoil is enhanced compared to the baseline airfoil. Further, the positive pressure on the lower surface is also greater in the case of optimal airfoil. Consequently, the C_l of optimal airfoil is higher than the baseline airfoil.

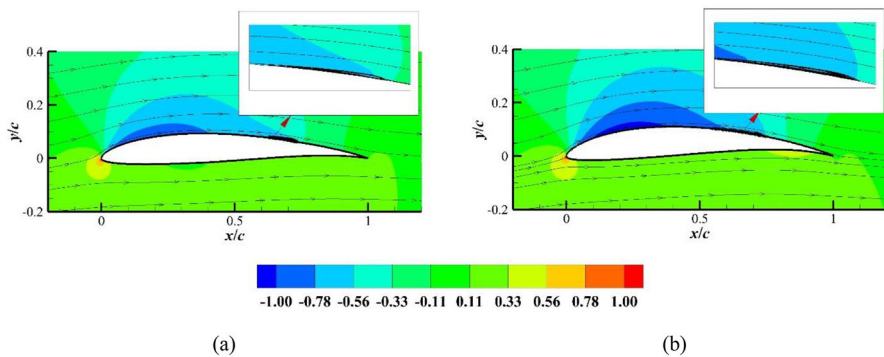


Fig. 9 Contours of C_p superimposed with streamlines; **a** baseline and **b** optimal geometry

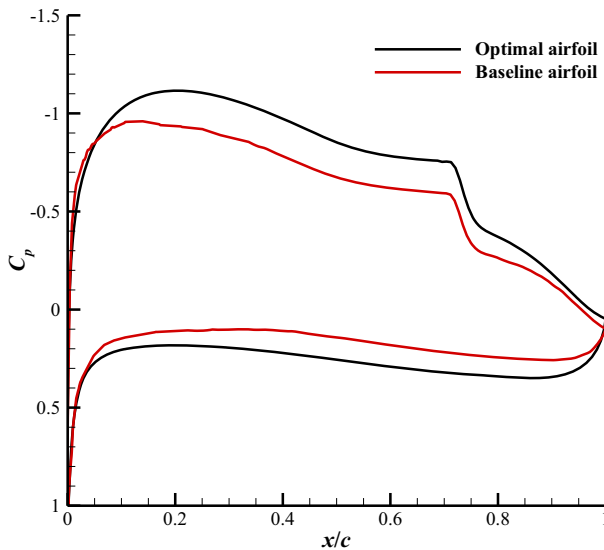


Fig. 10 Comparison of C_p distribution over baseline and optimal airfoils

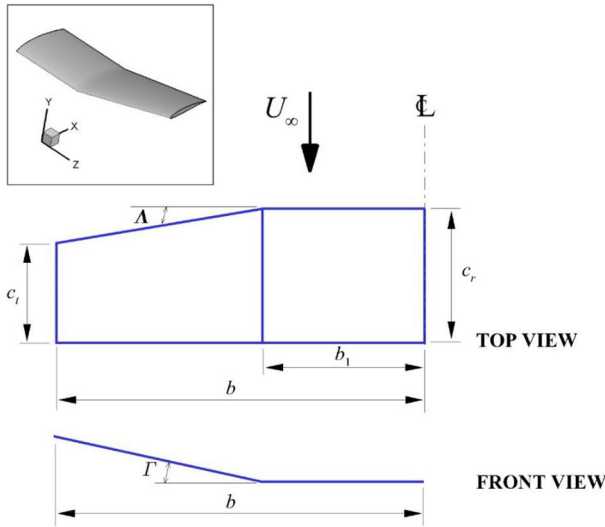


Fig. 11 Schematic sketch of baseline wing geometry; three-dimensional model of the wing is shown in the inset

4.2 Maximization of endurance factor of UAV wing

The second optimization problem considered is the maximization of the endurance factor of the wing of a small UAV. The flow conditions are $Re = 2.8 \times 10^5$, $\alpha = 5^\circ$, and $Tu = 0.1\%$. A sketch of this wing is shown in Fig. 11, with the three-dimensional model in the inset. The wing semi-span is denoted by b . The rectangular inboard wing is of span $b_1 = 0.4375b$. The outboard section of the wing is tapered and has a leading edge sweep of $\Lambda = 8.96^\circ$, and a dihedral of $\Gamma = 12^\circ$. The wing taper ratio, $\lambda = c_t/c_r$ is 0.7586, where c_r and c_t are the wing root and tip chord lengths, respectively. The wing has an aspect ratio of $AR = 5.93$. The wing is constructed of Eppler E214 airfoil.

The aerodynamic optimization problem is

$$\begin{aligned} & \max \left(\frac{C_L^{3/2}}{C_D} \right) \\ & \text{s. t. } \begin{cases} C_L \geq C_L^* \\ (t_{\max})_j \geq (t_{\max})_j^*, \quad j = 1, 2, \dots, 5 \end{cases} \end{aligned} \quad (16)$$

The endurance factor of the wing is to be maximized subject to one C_L and five thickness constraints at the five spanwise control stations. The lift coefficient corresponding to cruise condition of the UAV, $C_L^* = 0.80$ is chosen. The maximum thickness of the baseline airfoil is $t_{\max}^* = 0.111$. The constraints are absorbed in the objective function via penalty terms.

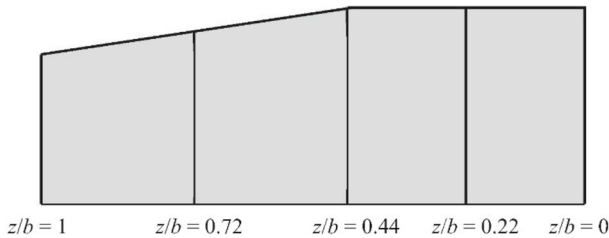


Fig. 12 Control stations along the span of the baseline wing

Five control stations are chosen along the wing semi-span, namely, $z/b = 0$ (wing root), $z/b = 0.22$, $z/b = 0.44$, $z/b = 0.72$, and $z/b = 1$ (wing tip), for wing geometry parameterization as shown in Fig. 12. At each of the spanwise stations the E214 airfoil is parameterized using Bézier curves as shown earlier in Fig. 4. Thus, at each control station there are six control points as design variables, and a total of 30 control points (5 stations \times 6 control points at each station) controlling the wing airfoil shape. The upper and lower bounds for variation of these design variables are $\eta_{i,j} \in [0.75 \eta_{bl}, 1.25 \eta_{bl}]$, where, $i = 1-6$ are the movable control points at each control station, and $j = 1-5$ are the spanwise stations. Further, three planform geometric parameters are included in the design optimization. They are: the rectangular portion of the wing b_1/b , leading edge sweep of the wing Λ , and wing dihedral Γ . These planform parameters are chosen as they are the independent variables. All the other planform variables are affected by the variation of these independent variables. For example, the tip chord is dependent on the variation of the leading-edge sweep. The planform area depends on the rectangular portion of the wing and leading-edge sweep. The bounds for these planform geometric design variables are $b_1/b \in [0, 1]$, $\Lambda \in [0, 18^\circ]$ and $\Gamma \in [0, 20^\circ]$, respectively. Thus, there is a total of 33 design variables making it a formidable wing design optimization problem.

The computational domain uses half of the wing due to symmetry in wing geometry about the mid-span. The computational domain inlet is set at a distance of $4b$ from the wing leading edge at root chord and the outlet is set at $8b$ behind the wing leading edge of the root chord. The spanwise extent of the domain is set at $3b$ from the symmetry plane. The computational domain used in the present study is shown in Fig. 13. The C–H type grid around the airfoil at the symmetry plane is swept along the span of the computational domain to generate the grid for the wing. A fine grid is used to resolve the boundary layers and away from the wall the grid is coarsened. The near wall $y^+ < 1$ for all the computations.

Computations are performed for a Reynolds number $Re = 2.8 \times 10^5$. This Re is calculated based on the mean aerodynamic chord of the wing and the UAV cruise velocity. The velocity inlet boundary condition is specified at the inlet of the computational domain. The pressure-outlet boundary condition is specified at the outlet of the computational domain. The no-slip boundary condition is applied on the wing surface. The computational procedure is the same as that employed for the airfoil computations as discussed in Sect. 4.1.

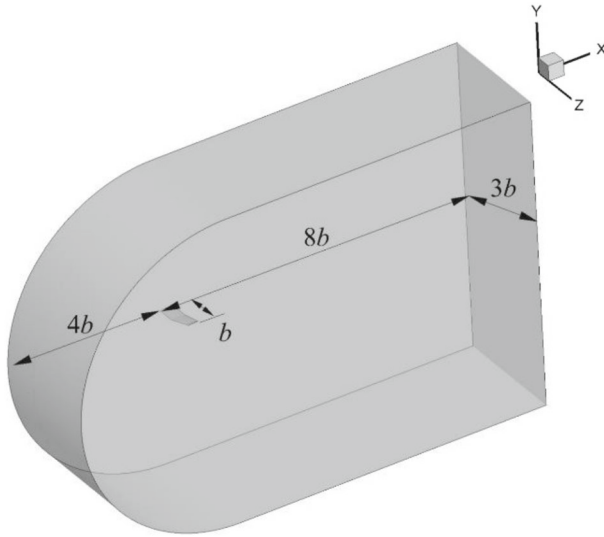


Fig. 13 Computational domain for wing computations

The optimization is performed using three levels of grids—namely, fine, medium and coarse grids as tabulated in Table 4. The grid on the symmetry plane and on the wing for these three grids are shown in Fig. 14. The endurance factor obtained from simulations of these three grids and the computational time are tabulated in Table 4.

The LHS technique is used to choose 200, 50 and 5 samples for the low-, medium- and high-fidelity CFD simulations, respectively. Computations are carried out for these samples using their respective grids. Hierarchical Kriging surrogate models are constructed for the wing endurance factor ($C_L^{3/2}/C_D$) as discussed in Sect. 2. The Pearson’s correlation coefficient values between high-to-medium, high-to-low, and medium-to-low fidelity models are 0.453, 0.965, and 0.277, respectively. The GA is used for obtaining the global optimum. Subsequently, EI infilling method is employed to update the MHK. High-fidelity computation is performed for the sample given by the EI, and the MHK models are updated in this manner until convergence of the objective function.

The optimal wing geometry is compared with the baseline wing in Fig. 15. The geometrical parameters of the wing planform are compared in Table 5. A striking

Table 4 Summary of grids used for wing optimization; $Re = 2.8 \times 10^5$, $Tu = 0.1\%$, $\alpha = 5^\circ$

Grid	No. of cells	C_L	C_D	$C_L^{3/2}/C_D$	Time (hours)
L1 (high-fidelity grid)	$260 \times 125 \times 180$	0.8060	0.04383	16.51	25
L2 (medium-fidelity grid)	$180 \times 100 \times 130$	0.8235	0.04514	16.56	8
L3 (low-fidelity grid)	$140 \times 75 \times 100$	0.8289	0.04549	16.59	4

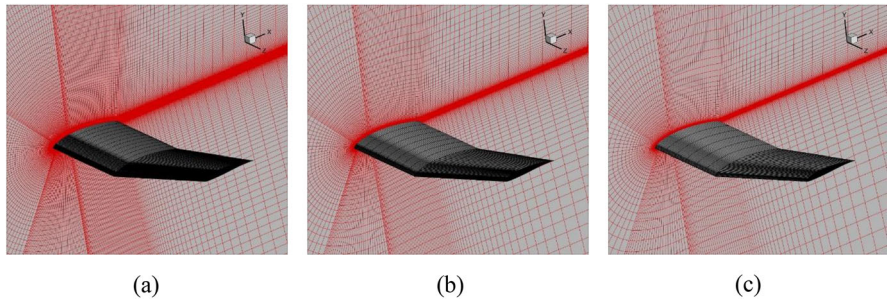


Fig. 14 Computational grids for wing; **a** high-, **b** medium-, and **c** low-fidelity grid

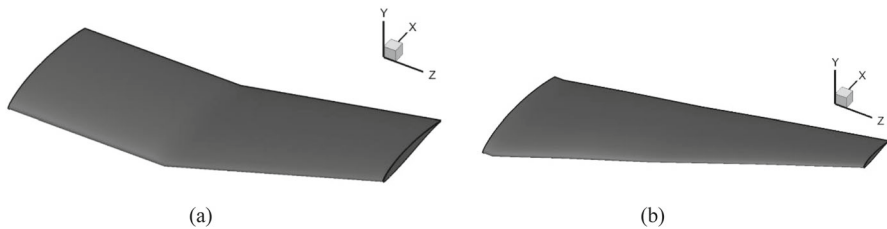


Fig. 15 Comparison of wing geometries **a** baseline and **b** optimal

Table 5 Comparison of geometrical parameters of the wing platform

Wing	b	b/b_1	Λ (deg)	Γ (deg)
Baseline	1	0.4375	8.96	12
Optimal	1	0.0288	13.62	11.32

geometrical feature of the optimal wing is the leading edge sweep right from the mid-span. The effect of sweep on the aerodynamic characteristics of wings in high-subsonic and supersonic flows is well-known (Anderson 2021; Vos and Farokhi 2015). However, in the present work, we obtain the swept wing as an optimal wing for incompressible flows at a low Reynolds number. Interestingly, the swept wing evolves as an optimum design. It must be mentioned that no special preference is given to the sweep angle as a design parameter; it is treated on par with all the other design variables in the design optimization problem. Further, nothing special is carried out in the optimization process to bias the optimal design towards swept wings. Thus, the evolution of the swept wing as an optimal design is truly remarkable. It may be noted that $\Lambda = 8.96^\circ$ for the baseline wing which has increased to $\Lambda = 13.62^\circ$ for the optimal wing. In our recent study (Patel et al. 2023), we performed comprehensive numerical simulations to evaluate the aerodynamic characteristics of the wing in Fig. 11 by systematically varying the wing geometric parameters. An interesting outcome of that study was that the wing with a leading edge sweep of $\Lambda = 17^\circ$ had the highest endurance

factor amongst the wing geometries investigated. The drag of that wing was 19.3 drag counts lower than the baseline wing. In the present study also we see similar trends. These results clearly demonstrate the beneficial effects of wing leading edge sweep on the aerodynamic characteristics of wings at low Reynolds numbers. This important outcome, we believe, will be useful to the designers of UAV wings.

The aerodynamic performance characteristics of the baseline and optimal wings are compared in Table 6. The C_L of the optimal wing is higher than the baseline wing. The C_D of the optimal wing is a substantial 45 drag counts lower than the baseline wing. The major drag reduction comes from the pressure drag component being reduced from 0.03860 for the baseline wing to 0.03342 for the optimal wing. The lift-to-drag ratio, another important aerodynamic performance metric, is increased by 12.1%. Finally, the endurance factor of the optimal wing is 12.5% higher compared to the baseline wing. These improvements in the aerodynamic parameters are substantial considering the fact that baseline wing itself is of good aerodynamic design having been designed by experienced designers.

The contours of C_p superimposed with limiting streamlines on the upper surface of the baseline and optimal wings are compared in Fig. 16. The enhanced suction pressure ($C_p \sim -0.96$ to -1.20) in the leading edge region of the optimal wing is clearly seen in the contour plots. The higher suction region spans almost the entire wing span of the swept optimal wing. The C_p distribution at the five spanwise stations are plotted in Fig. 17 for both the baseline and optimal wings. It is seen that the suction pressure peak of optimal wing at stations 2, 3, 4, and 5 is higher compared to the baseline sections. The lift generated at the tip section is reduced in the case of optimal wing.

The spanwise lift distribution of the baseline and optimal wings are compared in Fig. 18. In this figure the variation of the local section lift coefficient, non-

Table 6 Aerodynamic characteristics of baseline and optimal wings

Wing	C_L	C_D	C_L/C_D	$C_L^{3/2}/C_D$
Baseline	0.8060	0.04383	18.39	16.51
Optimal	0.8113	0.03936	20.61	18.57

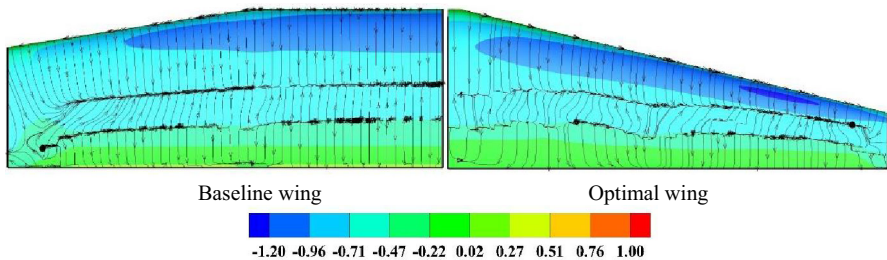


Fig. 16 Comparison of C_p contours superimposed with limiting streamlines on the upper surface of baseline (left frame) and optimal (right frame) wings

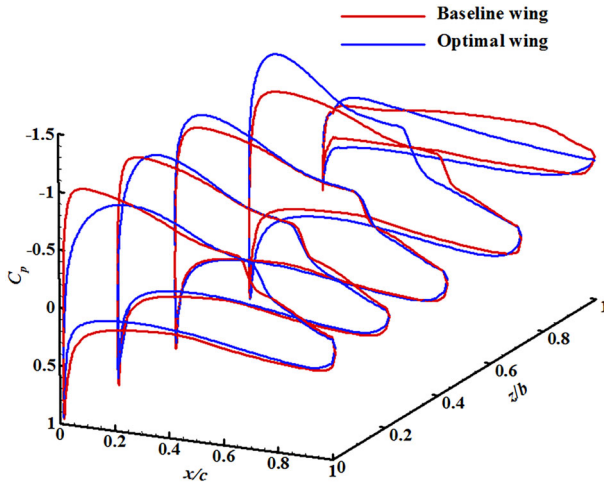


Fig. 17 Comparison of C_p distribution over baseline and optimal wings

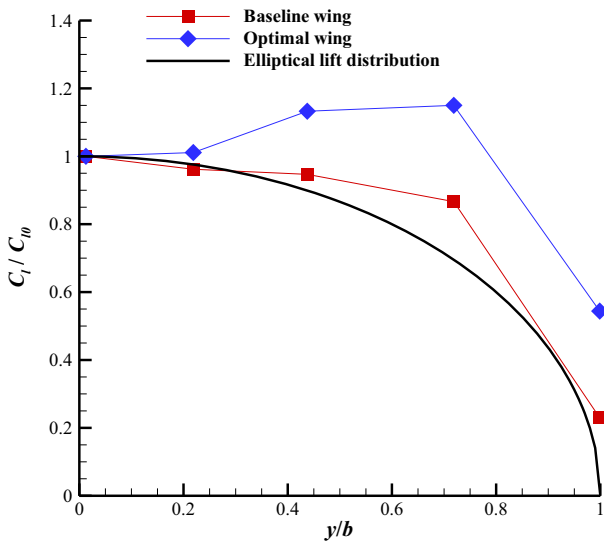


Fig. 18 Spanwise lift distribution of baseline and optimal wings

dimensionalized by the lift coefficient at the wing root, along the wing span is plotted. The classical elliptical lift distribution (Katz and Plotkin 2001) is also plotted in Fig. 18 for comparison. It is interesting to note that both the baseline and optimal wings produce higher C_l than the equivalent elliptic loading. It may be recalled that the baseline wing itself had an outboard leading edge sweep of $\Lambda = 8.96^\circ$ (see Fig. 11). It is seen that at the inboard section both the wings produce nearly the same sectional C_l . However, the effect of sweep on the local lift coefficient is striking in the outboard portion

of optimal wing. The optimal wing produces substantially higher C_l than the baseline wing in the outboard region for $y/b \geq 0.44$, reiterating the aerodynamic benefits of wing sweep.

Some comments regarding the wing sweep in the low Reynolds number range in the literature are in place here. Yen and Huang (2011) found that the maximum lift coefficient of a swept wing increased by approximately 45% compared to the unswept wing based on their experiments. Chen and Qin (2013) concluded that a swept wing with an 18° leading edge sweep exhibited the highest lift coefficient; they also noted that the loading was greater near the wing tips. Our current findings support their conclusions. Okamoto and Azuma (2011) conducted experimental research on the effects of sweep on the aerodynamic characteristics of wings at Reynolds number about 1×10^4 to understand insect flight. This Reynolds number regime is termed ultra-low. Even at these low Reynolds numbers, they observed that the maximum lift coefficient increased with an increasing sweep angle, particularly at high angles of attack. It is important to note that in our present study, we limited the sweep angle to 18° , based on our recent computations (Rajiv and Sivapragasam 2024). In that study, we found that the lift coefficient at cruise condition of the UAV decreased after $\Lambda = 10^\circ$; hence, we set the range of sweep angles $\Lambda \in [0^\circ, 18^\circ]$ in the current work. The present optimization is performed for the UAV cruise condition. It is possible that other sweep angles may be optimal at other flight conditions. A multi-point optimization should be carried out to account for this. The present MHK-based optimization methodology can readily be extended for such optimization problems.

5 Conclusions

The Multi-Level Hierarchical Kriging (MHK) surrogate model has been implemented for constrained aerodynamic shape optimization in the low Reynolds numbers regime. In this Reynolds number regime the boundary layer undergoes laminar separation, transition to turbulence of the separated shear layer, and turbulent flow reattachment on the surface. The Reynolds numbers chosen in the present study are conducive to promote flow transition and possible reattachment. Further, the flow at such low Reynolds numbers are extremely sensitive to the design parameters. For example, if the flow field exhibits a laminar separation bubble for a set of design parameters, and for only a small perturbation in the design variables, the laminar separation bubble completely disappears with a fully separated flow, leading to substantial changes in aerodynamic force coefficients that are to be optimized. Hence the optimization methodology should be robust to account for these sensitivities. It is remarkable that the MHK-based optimization methodology implemented in the present study is able to achieve this.

The application of the MHK modeling approach resulted in an efficient and a robust optimization framework. The efficacy of the MHK modeling framework was first demonstrated on a three-level Branin function. Subsequently, the MHK methodology was applied to improve the aerodynamic characteristics in the low Reynolds numbers regime. The endurance factor of the Eppler E214 airfoil improved by 28%. Next, an optimization study was performed to improve the endurance factor of an UAV wing

using the MHK method. The optimal wing had leading edge sweep starting from the wing mid-span. Though the effects of sweep on the aerodynamic characteristics of wings at high subsonic and supersonic Mach numbers is well known, the wing sweep evolves as an optimal wing in low Reynolds number flow regime in the present study. In the present optimization procedure, no special status is accorded to the wing sweep angle as a design variable; it is treated on par with all the other design variables. Further, no special processing is carried out in optimization procedure to handle the wing sweep angle. The fact that the swept wing evolves as an optimal wing is indeed remarkable, and is a novel contribution of the present paper. These results will be beneficial to UAV designers. The endurance factor of the optimal wing had improved by 12.5%. The drag coefficient was reduced by 45 drag counts. The present optimization methodology can be readily extended to full aircraft configurations and also for other expensive engineering functions particularly when variable fidelity data is available.

Acknowledgements We acknowledge the productive discussions with the scientists of the Aerodynamics Division, Aeronautical Development Establishment, Bangalore. We thank A. Vadivelan and G. Sankar, Aeronautical Development Establishment, for their active involvement and valuable contributions to this work.

Author contributions MS conceptualized the optimization framework and the computational procedures, while KSR implemented the optimization. AD and ANA carried out the simulations and optimization of the airfoil and wing, respectively. MS wrote the manuscript. All authors read and approved the final manuscript.

Funding This project was supported by the grant-in-aid funding from the Aerodynamics Panel, Aeronautics Research and Development Board, Defence Research and Development Organisation, India, under the Project Number 1924 (ARDB/01/1031924/M/I).

Data availability The data that support the findings of this study are available from the corresponding author upon reasonable request.

Declarations

Competing interests The authors declare no competing interests.

Ethics approval and consent to participate This manuscript does not contain human and/or animal studies, hence ethics approval and consent to participate are not applicable.

Consent for publication This manuscript does not contain any individual person's data in any form, hence consent to participate is not applicable.

References

- Amoignon OG, Pralits JO, Hanifi A, Berggren M, Henningson DS (2006) Shape optimization for delay of laminar–turbulent transition. *AIAA J* 44:1009–1024
- Anderson JD (2021) *Modern compressible flow: with historical perspective*, 4th edn. McGraw Hill, New York
- Arshad A, Rodrigues LB, López IM (2021) Design optimization and investigation of aerodynamic characteristics of low Reynolds number airfoils. *Int J Aeronaut Space Sci* 22:751–764
- Austin R (2010) *Unmanned aircraft systems*. Wiley, Chichester
- Cameron L, Early J, McRoberts R (2011) Metamodel assisted multi-objective global optimisation of natural laminar flow aerofoils. *AIAA Paper* 2011–3001
- Carmichael BH (1981) *Low Reynolds number airfoil survey*. NASA CR-165803

- Chen ZJ, Qin N (2013) Planform effects for low-Reynolds-number thin wings with positive and reflex cambers. *J Aircr* 50:952–964
- Chen Y, Rao H, Xiong N, Fan J, Shi Y, Yang T (2023) Adjoint-based robust optimization design of laminar flow airfoil under flight condition uncertainties. *Aerosp Sci Technol* 140:108465
- Chi J, Han ZH, Fan T, Song WP (2019) Hybrid inverse/optimization design approach for transonic natural-laminar-flow airfoils. *AIAA Paper* 2019–1475
- Das A, Sivapragasam M (2024) Variable-fidelity surrogate model-based airfoil optimization at a moderate Reynolds number. *J Aerosp Sci Technol* 76:1–12
- Driver J, Zingg DW (2007) Numerical aerodynamic optimization incorporating laminar–turbulent transition prediction. *AIAA J* 45:1810–1818
- Forrester AIJ, Keane AJ (2009) Recent advances in surrogate-based optimization. *Prog Aerosp Sci* 45:50–79
- Forrester AIJ, Sóbester A, Keane AJ (2007) Multi-fidelity optimization via surrogate modelling. *Proc R Soc a: Math, Phys Eng Sci* 463:3251–3269
- Forrester AIJ, Sóbester A, Keane AJ (2008) *Engineering design via surrogate modelling: a practical guide*. John Wiley, Chichester
- Gaster M (1967) The structure and behaviour of laminar separation bubbles. *Aeronautical Research Council Reports and Memoranda* 3595
- Gundlach J (2012) *Designing unmanned aircraft systems: a comprehensive approach*. AIAA, Reston
- Halila GLO, Martins JRRA, Fidkowski KJ (2020) Adjoint-based aerodynamic shape optimization including transition to turbulence effects. *Aerosp Sci Technol* 107:106243
- Han ZH, Goertz S (2012) Hierarchical kriging model for variable-fidelity surrogate modeling. *AIAA J* 50:1285–1296
- Han ZH, Chen J, Zhang KS, Xu ZM, Zhu Z, Song WP (2018) Aerodynamic shape optimization of natural-laminar-flow wing using surrogate-based approach. *AIAA J* 56:2579–2593
- Han ZH, Xu C, Zhang L et al (2020) Efficient aerodynamic shape optimization using variable-fidelity surrogate models and multilevel computational grids. *Chin J Aeronaut* 33:31–47
- Han ZH, Deng J, Liu J, Zhang KS, Song WP (2012) Design of laminar supercritical airfoils based on Navier–Stokes equations. *Proc. 28th Congress of the International Council of the Aeronautical Sciences, ICAS Paper ICAS2012–2.2.2*, Brisbane, Australia
- He Z, Xiong X, Yang B, Li H (2020) Aerodynamic optimisation of a high-speed train head shape using an advanced hybrid surrogate-based nonlinear model representation method. *Optim Eng* 23:59–84
- Hicks RM, Henne PA (1978) Wing design by numerical optimization. *J Aircr* 15:407–412
- Horton HP (1968) *Laminar separation bubbles in two and three dimensional incompressible flow*. Ph. D. Thesis, University of London
- Jameson A (1988) Aerodynamic design via control theory. *J Sci Comput* 3:233–260
- Jayaraman J (2014) *Unmanned aircraft systems: a global view*. DRDO, New Delhi
- Jones DR (2001) A taxonomy of global optimization methods based on response surfaces. *J Glob Optim* 21:345–383
- Jones D, Schonlau M, Welch W (1998) Efficient global optimization of expensive black-box functions. *J Glob Optim* 13:455–492
- Katz J, Plotkin A (2001) *Low-speed aerodynamics*, 2nd edn. Cambridge University Press, Cambridge
- Kennedy MC, O’Hagan A (2000) Predicting the output from a complex computer code when fast approximations are available. *Biometrika* 87:1–13
- Khayatzadeh P, Nadarajah S (2012) Aerodynamic shape optimization of natural laminar flow (NLF) airfoils. *AIAA Paper* 2012–0061
- Krige DG (1951) A statistical approach to some basic mine valuations problems on the Witwatersrand. *J Chem Metall Min Eng Soc South Afr* 52:119–139
- Langtry RB, Menter FR (2009) Correlation-based transition modeling for unstructured parallelized computational fluid dynamics codes. *AIAA J* 47:2894–2906
- Lee JD, Jameson A (2009) Natural-laminar-flow airfoil and wing design by adjoint method and automatic transition prediction. *AIAA Paper* 2009–0897
- Leifsson L, Koziel S (2015) *Simulation-driven aerodynamic design using variable-fidelity models*. Imperial College Press, London
- Li H, Jiang S, Yang P, Zhang K (2022) The numerical prediction and optimization design of natural laminar flow airfoil for UAV. *Proc of 2022 International Conference on Autonomous Unmanned Systems ICAUS 2022*, Ed: Fu W, Gu M, Niu Y

- Lissaman PBS (1983) Low-Reynolds-Number Airfoils *Ann Rev Fluid Mech. Annu Rev Fluid Mech* 15:223–239
- Marshall DM, Barnhart RK, Shappe E et al (eds) (2016) Introduction to unmanned aircraft systems, 2nd edn. CRC Press, Boca Raton
- Menter FR (1994) Two-equation eddy-viscosity turbulence models for engineering applications. *AIAA J* 32:1598–1605
- Morris MD, Mitchell TJ (1995) Exploratory designs for computational experiments. *J Stat Plan Inference* 43:381–402
- Mueller TJ, DeLaurier JD (2003) Aerodynamics of small vehicles. *Ann Rev Fluid Mech* 35:89–111
- Nie H, Song WP, Han ZH, Chen J, Tu G (2022) A surrogate-based e^N method for compressible boundary-layer transition prediction. *J Aircr* 59:89–102
- Okamoto M, Azuma A (2011) Aerodynamic characteristics at low Reynolds numbers for wings of various planforms. *AIAA J* 49:1135–1150
- Patel KR, Rao KS, Sivapragasam M (2023) Aerodynamic performance of an unmanned aerial vehicle wing for varied wing geometric parameters. *J Aerosp Sci Technol* 75:270–289
- Perdikaris P, Raissi M, Damianou A et al (2017) Nonlinear information fusion algorithms for data-efficient multi-fidelity modelling. *Proc R Soc a: Math, Phys Eng Sci* 473:20160751
- Piotrowski MG, Zingg DW (2022) Investigation of a smooth local correlation-based transition model in a discrete-adjoint aerodynamic shape optimization algorithm. *AIAA Paper* 2022–1865
- Pranesh C, Sivapragasam M, Narahari HK (2018) Multi-fidelity aerodynamic shape optimization of an airfoil at transitional low Reynolds number. National Conference on Multidisciplinary Design, Analysis, and Optimization, Indian Institute of Science, Bangalore, 23–24 March 2018
- Priyanka R, Sivapragasam M (2021) Multi-fidelity surrogate model-based airfoil optimization at a transitional low Reynolds number. *Sādhanā Proc Indian Acad Sci* 46:0058
- Queipo NV, Haftka RT, Shyy W et al (2005) Surrogate-based analysis and optimization. *Prog Aerosp Sci* 41:1–28
- Qui Y, Yuan Y, Yu R et al (2022) Aerodynamic shape optimization of porous fences with curved deflectors using surrogate modelling. *Optim Eng* 24:2387–2408
- Rajiv VR, Sivapragasam M (2024) Aerodynamics of leading edge swept wings at low Reynolds number. under preparation
- Rashad R, Zingg DW (2016) Aerodynamic shape optimization for natural laminar flow using a discrete-adjoint approach. *AIAA J* 54:3321–3337
- Sabater C, BekemeyerGörtz Stefan P (2022) Robust design of transonic natural laminar flow wings under environmental and operational uncertainties. *AIAA J* 60:767–782
- Sacks J, Welch WJ, Mitchell TJ et al (1989) Design and analysis of computer experiments. *Stat Sci* 4:409–423
- Samareh JA (2001) Survey of shape parameterization techniques for high-fidelity multidisciplinary shape optimization. *AIAA J* 39:877–884
- Selig MS, Donovan JF, Fraser DB (1989) Airfoils at low speeds. H. A. Stokely, Virginia
- Shi Y, Mader CA, He S, Halila GLO, Martins JRRR (2020) Natural laminar-flow airfoil optimization design using a discrete adjoint approach. *AIAA J* 58:4702–4722
- Shi Y, Mader CA, Martins JRRR (2021) Natural laminar flow wing optimization using a discrete adjoint approach. *Struct Multidiscip Optim* 64:541–562
- Shyy W, Lian Y, Tang J et al (2008) Aerodynamics of low Reynolds number flyers. Cambridge University Press, Cambridge
- Sudhi A, Radespiel R, Badrya C (2023) Design exploration of transonic airfoils for natural and hybrid laminar flow control applications. *J Aircr* 60:716–732
- Surjanovic S, Bingham D (2013) Virtual library of simulation experiments: test functions and datasets. <http://www.sfu.ca/~ssurjano/optimization.html>. Accessed 24 Oct 2022
- Tani I (1964) Low-speed flows involving bubble separations. *Prog Aerosp Sci* 5:70–103
- Toal D, Bressloff N, Keane A (2008) Kriging hyperparameter tuning strategies. *AIAA J* 46:1240–1252
- Vos R, Farokhi S (2015) Introduction to transonic aerodynamics. Springer, Heidelberg
- Wang S, Guo Z (2022) Robust optimization of natural laminar flow airfoil based on random surface contamination. *Appl Sci* 12:8757
- Wauters J, Degroote J (2021) Surrogate-assisted parametric study of a wing fence for unmanned aerial vehicles. *J Aircr* 58:562–579
- Xu CZ, Han ZH, Zan BW, Zhang KS, Chen G, Wang WZ (2024) Expert’s experience-informed hierarchical kriging method for aerodynamic data modeling. *Eng Appl Artif Intell* 133:108490

- Yan C, Zhang Y, Zhang M (2023) Numerical optimization of transonic natural laminar flow nacelles. *Chin J Aeronaut* 36:35–51
- Yen SC, Huang LC (2011) Reynolds number effects on flow characteristics and aerodynamic performances of a swept-back wing. *Aerosp Sci Technol* 15:155–164
- Yu H, Zhao Y, Feng W, Zhao C, Feng Y, Mao S, Zhao L (2023) Research on optimization design of low reynolds number airfoils based on CFD. *Proc of the 6th China Aeronautical Science and Technology Conference (CASTC 2023)*
- Zadeh PM, Mehmani A, Messac A (2016) High fidelity multidisciplinary design optimization of a wing using the interaction of low and high fidelity models. *Optim Eng* 17:503–532
- Zhang YF, Fang X, Chen HX, Fu S, Duan Z, Zhang Y (2015) Supercritical natural laminar flow airfoil optimization for regional aircraft wing design. *Aerosp Sci Technol* 43:152–164
- Zhang Y, Han ZH, Song WP (2024) Multi-fidelity expected improvement based on multi-level hierarchical kriging model for efficient aerodynamic design optimization. *Eng Opt*. <https://doi.org/10.1080/0305215X.2024.2310182>

Publisher's Note Springer Nature remains neutral with regard to jurisdictional claims in published maps and institutional affiliations.

Springer Nature or its licensor (e.g. a society or other partner) holds exclusive rights to this article under a publishing agreement with the author(s) or other rightsholder(s); author self-archiving of the accepted manuscript version of this article is solely governed by the terms of such publishing agreement and applicable law.